PUBLICATION

MUSTANG

A MUltiple Space and Time scale Approach for the quaNtification of deep saline formations for CO_2 storaGe

Project Number:227286

AUTHORS: *D. Stevens, H. Power, J. Polanco, A. Cliffe*

TITLE: *A high-resolution local RBF collocation method for steady-state poroelasticity and hydromechanical damage analysis*

The research leading to these results has received funding from the European Community's Seventh Framework Programme [FP7/2007/2013) under grant agreement n° [227286]

Status	AUTHOR VERSION
Date	2014
Publisher	Willey Online Library
Reference	International Journal for Numerical and Analytical Methods in Geomechanics, DOI: 10.1002/nag.2317, 2014

A High-Resolution Local RBF Collocation Method for Steady-State Poroelasticity and Hydromechanical Damage Analysis

D. Stevens[+], *H. Power*[+*], *J. Polanco*[%], *A. Cliffe*[#]

[+] Faculty of Engineering, Division of Energy and Sustainability, University of Nottingham, UK

[%] École Polytechnique, 91128 Palaiseau, France

[#] Faculty of Mathematics, University of Nottingham, UK

[*] Correspondence Author: H. Power, henry.power@nottingham.ac.uk

Abstract

In this work we describe a meshless numerical method based on local collocation with radial basis functions (RBFs), for the solution of the poroelasticity equation. The RBF finite collocation approach (RBF-FC) forms a series of overlapping nodal stencils, over which an RBF collocation is performed. These local collocation systems enforce the governing PDE operator throughout their interior, with the inter-system communication occurring via the collocation of field variables at the stencil periphery. The method does not rely on a generalised finite differencing approach, whereby the governing partial differential operator is reconstructed at the global level to drive the solution of the PDE. Instead, the PDE governing and boundary operators are enforced directly within the local RBF collocation systems, and the sparse global assembly is formed by reconstructing the value of the field variables at the centrepoint of the local stencils. In this way, the solution of the PDE is driven entirely by the local RBF collocation, and the method more closely resembles the approach of the full-domain RBF collocation method. By formulating the problem in this fashion, high rates of convergence may be attained without the computational cost and numerical ill-conditioning issues that are associated with the full-domain RBF collocation approach.

An analytical solution is formulated for a 2D poroelastic fluid injection scenario, and is used to verify the proposed implementation of the method. Highly accurate solutions are produced, and convergence rates in excess of sixth order are observed for each field variable (i.e. pressure and displacement), and field-variable derivative (i.e. pressure gradients and stresses). The stress and displacement fields resulting from the solution of the poroelasticity equation are then used to describe the formation and propagation of micro-fractures and micro-fissures, which may form in the presence of large shear strain, in terms of a continuous damage variable which modifies the mechanical and hydraulic properties of the porous medium. The formation of such hydromechanical damage, and the resulting increase in hydraulic conductivity, is investigated for a pressurised injection into sandstone.

-
KEYWORDS: Meshless, RBF, poroelasticity, analytical solution, hydromechanical damage

1 Introduction and motivation

RBF collocation methods for the solution of PDEs, originally described by Kansa [1, 2], are attractive due to their meshless formulation, relative ease of implementation, high convergence rates, and flexibility with regards the enforcement of arbitrary boundary operators. However the use of globally supported basis functions leads to fully-populated collocation matrices, which become increasingly ill-conditioned and computationally expensive with increasing dataset size. These limitations have in recent years motivated researchers to investigate various methods for restricting the domain of support for the basis functions; thereby mitigating the computational cost and numerical conditioning issues while maintaining the performance and flexibility of the full-domain formulation.

RBF localisations typically fall into two categories; methods based on compactly supported basis functions, and methods using connected networks of local collocation systems. The concept of compactly supported basis functions was introduced by Wu [3], and extended by Wendland [4, 5]. The compact support principle uses radial basis functions that are truncated so as to be non-zero only within a local radius, resulting in a collocation system that is only sparsely populated. While compact-support RBF collocation is an excellent approach for the interpolation of scattered data, it is less well suited to the solution of PDEs, requiring the radius of support to be maintained as the dataset density increases in order to maintain convergence rates [ref]. In this way the bandwidth of the collocation matrix increases with the dataset density. The alternative approach of defining networks of small, connected RBF collocation systems has been in use since 2001 (see [6]). While this approach is somewhat more complex than the compact support RBF approach, it allows for much greater flexibility in the specific method of implementation, and has led to many interesting adaptations across a wide range of problems.

One such local RBF approach, which is popular in the literature, is the generalised finite difference approach (RBF-FD); see for example [7, 8, 9, 10, 11]. In this approach the RBF interpolants take the place of polynomials in the traditional finite difference method, with the governing and boundary partial differential operators reconstructed from the interpolating RBFs in order to form a sparse global system. By replacing the polynomials with RBFs the method is able to operate on irregular datasets; however, many desirable features of the full-domain RBF approach may be lost in this formulation. We propose instead to use an RBF localisation that is more closely related to the full-domain approach. Rather than reconstructing an approximation of the governing PDE at the global assembly level, as is the case in both traditional and RBF-based finite differencing approaches, the RBF "finite collocation" approach (RBF-FC) enforces the governing and boundary PDE operators directly within the local RBF collocation systems, and assembles only the values of the field variables into the sparse global assembly. In this way the RBF-FC approach does not rely on a generalised finite differencing procedure; instead the solution of the PDE is driven entirely via collocation of the relevant operators within the local RBF systems.

In the proposed RBF-FC approach, the computational domain is discretised by a quasi-scattered distribution of nodes, with each internal node connected to its neighbours in some suitable fashion to form a series of local stencils. Over each stencil an RBF collocation is performed. At the stencil interior the linearised PDE is enforced within the RBF collocation, and at the stencil boundaries the

unknown value of the solution field is collocated via a Dirichlet operator. The unknown values of the solution field are then reconstructed at each interior node, in terms of the unknown values of the field variable at surrounding nodes. These nodal values are then assembled into a sparse global system, which may be solved to obtain the solution field over the entire solution domain. The stencils therefore communicate only via their respective boundaries, and in this way the structure of the local collocation systems closely resembles the global RBF collocation approach. The localisation of the method, however, significantly mitigates the computational cost and numerical conditioning issues that are typically associated with full-domain RBF methods on large datasets.

This RBF finite collocation (RBF-FC) principle was originally described in [12] for the solution of convection-diffusion and linear elasticity problems. The inclusion of the PDE governing and boundary operators within the collocation systems allows for many beneficial features, and for improved solution accuracy, in comparison to approaches that use unmodified radial basis functions as interpolants. For example, the problem of a thin plate with a circular hole under uniform axial traction is solved in [13] using a cell-based smoothed RBF approach, which uses 'native' RBF interpolants. A variety of RBF stencil configurations are investigated, resulting in convergence rates of between 1.73 and 2.43 for displacement, and between 0.87 and 1.19 for stresses on this problem. The same problem is also solved in [12] using the RBF-FC approach, demonstrating convergence rates above 6.5 in displacement, and in all stress components. The improved convergence rates, and the ability to reconstruct partial derivatives at the same accuracy as the solution field itself, are properties that arise from the inclusion of the PDE governing and boundary operators into the local collocation systems. In the present work the RBF-FC method is formulated for the solution of the linear poroelasticity equation, and for the nonlinear growth of hydromechanical damage. The formulation of the RBF-FC approach for steady poroelastic analysis is described fully in Section 4.

Hydromechanical processes generally play an important role in geological media. These formations are usually fluid-saturated fractured rock masses. Therefore, they can deform either as a result of changes in external loads or internal pore pressures. The use of coupled hydromechanical models allow determination of the conditions under which mechanical failure (shear failure or hydraulic fracture) can occur. In the case of CO2 injection into deep saline aquifers, such analysis allows constraints to be placed on injection pressures such that damage to critical parts of the surrounding geology can be limited to below an acceptable fracturing threshold.

In poroelasticity, the governing equation describing rock deformation is defined by a non-homogeneous Navier equation for linear elasticity, with the non-homogeneous term proportional to the gradient of the fluid pressure. Similarly, the stress tensor constitutive equation is given by the linear elastic stress tensor minus the fluid pressure. The fluid mass balance equation occupying the void space must also take into to account the motion due to the solid deformation, resulting in a set of coupled partial differential equations.

An elegant description of the damage processes in porous rock due to the injection of over pressurized fluid is given in [14], from which we take some relevant remarks. The classical theory of poroelasticity, which is based on linear elastic behaviour, can have a significant limitation in the application to geomaterials, which could exhibit irreversible and non-linear phenomena in the behaviour of the soil skeleton. These non-linear phenomena in most natural brittle geomaterials can range from the generation of microcracks (i.e. damage) to the development of macrocracks (i.e. fractures). The generation of these flaws in solid matrices can alter the deformability and permeability characteristics of the saturated geomaterials. The description of the dominant mode of the flaw should include: the state of stress, rate of loading, microstructure of the geomaterial, presence of stress singularities (e.g.

sharp contacts) and the ability of a flaw to open and close. The notion of continuum damage can be more relevant to semibrittle geomaterials such as soft rocks, over consolidated sandstone and other porous geological media where softening due to generation of microvoids or microcracks exist.

The development of microcracks and microvoids alters the elastic stiffness of the porous skeleton. A concurrent effect of such damage processes is the change of the permeability of the porous medium (which increases), resulting in an easy migration of the fluid within the saturated material. The gradual degradation in the elastic stiffness and the change to hydraulic conductivity is a result of either continuing growth of existing microdefects, or the progressive nucleation of new microdefects. For a given state of stress, the extent of damage is an intrinsic property of the material which is defined by the damage evolution process.

In contrast to discrete fractures, the micromechanical damage of porous skeleton does not result in any discontinuity in displacement, traction and fluid pressure fields within the porous medium. Also, the damage effects are governed by the global state of stresses in the porous medium, and consequently the process can be analysed by including the concept of continuum damage mechanics [15] into the classical theory of poroelasticity. This is achieved by representing the stiffness properties and permeability characteristics of a porous medium as a function of the state of damage in the material. The continuum damage model examines the development of microcracks, or any other microdefects, prior to the development of macrocracks (i.e. fractures). The process of damage is expected to be highly anisotropic in nature and could be restricted to localised zones.

The theory of continuum damage mechanics has been widely used to predict the nonlinear response of a variety of materials, including metals, concrete, composites, and geological materials; see [16, 17, 18, 19, 20] among others. The nonlinear behaviour of materials is considered by introducing local damage variables in the analysis. The damage variables represent the average material degradation at the macro-scale that are normally associated with the classical continuum description. In this way, the damage concept can be easily incorporated into the theory of poroelasticity.

The development of damage, including initiation and coalescence of microcracks, gives rise to nonlinear phenomena in the constitutive behaviour of fluid saturated geomaterials. The effect of damage on either the degradation of elastic moduli or strength (in the form of strain softening) of geomaterials such as rocks has been observed by [21] and [22]. The effect of microcrack generation on the permeability of saturated geomaterials has also been observed by [23], [24] and [25]. More recently the theory of the continuous damage of fracture mechanics has been applied by [26] to solve problems related to hydraulic fracturing in heterogeneous geo-materials.

The present work is ultimately motivated by the risk analysis of possible leakage during CO2 injection into deep saline aquifers, due to the localised rise in pressure produced by the injection of fluid. Even when a total failure of the rock does not occur, the presence of material damage will result in larger values of the effective rock permeability, with an associated increase in the rate of leakage for a given imposed pressure gradient. The increase in rock permeability can be as critical as a total failure of the cap rock, due to the corresponding increase of leakage. Although we are ultimately motivated by the problem of cap rock integrity during CO2 sequestration into deep saline aquifers, in this work we do not attempt to fully solve this type of problem. Instead we present a novel and robust numerical technique that can be used in the analysis of such complex problems, and demonstrate its application with relatively simple 2D numerical examples that describe the local evolution of damage during an injection scenario.

2 Linear Poroelasticity

The theory of poroelasticity was essentially developed by Maurice A. Biot. In [27] he couples Navier's linear elasticity equations with Darcy's law for the flow through a porous medium. For an isotropic material and incompressible fluid the equations modelling the displacement u_i of the material and the pressure p of the fluid can be written as:

$$\frac{\partial}{\partial x_i}\left(k_{ij}\left(x\right)\frac{\partial\left(p-\rho g\, x_2\right)}{\partial x_j}\right)=\frac{\partial\varepsilon}{\partial t}+\eta S_0\frac{\partial p}{\partial t} \tag{1}$$

where the average seepage velocity, v_i, is described by the Darcy law in terms of the gradient of the pressure field p with hydraulic conductivity $k_{ij}\left(x\right)$. In the above equation, ρ is the fluid density, g the gravitational acceleration, η the porosity, S_o the fluid compressibility coefficient, ε is the dilatational strain $\frac{\partial u_j}{\partial x_j}$ for a displacement u_i in the porous medium, and x_2 is the vertical coordinate taken positive upwards.

The poroelastic stress tensor is given by

$$\sigma_{ij}=\lambda\varepsilon_{kk}\delta_{ij}+2\mu\varepsilon_{ij}-\alpha p\delta_{ij} \tag{2}$$

where $\alpha\in[0,\,1]$ is the Biot coefficient, ε_{ij} is the infinitesimal strain tensor

$$\varepsilon_{ij}=\frac{1}{2}\left(\frac{\partial u_i}{\partial x_j}+\frac{\partial u_j}{\partial x_i}\right) \tag{3}$$

and λ, μ are the Lame constants which, for a plane-strain assumption, are related to the Young's modulus (E) and the Poisson ration (ν) as:

$$\lambda=\frac{E\nu}{\left(1+\nu\right)\left(1-2\nu\right)},\qquad\mu=\frac{E}{2\left(1+\nu\right)} \tag{4}$$

The stress field satisfies the Navier momentum equation

$$\frac{\partial\sigma_{ij}}{\partial x_j}=0 \tag{5}$$

Writing the stress tensor in terms of the effective stress as

$$\sigma_{ij}=\widetilde{\sigma}_{ij}-\alpha p\delta_{ij} \tag{6}$$

and substituting into equation (5), the following non-homogeneous equation is found:

$$\frac{\partial\widetilde{\sigma}_{ij}}{\partial x_j}=\alpha\frac{\partial p}{\partial x_i} \tag{7}$$

where the pressure field and its gradient are computed from the solution of the Darcy flow equation (1), and are coupled with the elasticity equation. In this way a system of coupled partial differential equations, (1) and (7), determine the displacement u_i of the material and the fluid pressure p, via two-way coupling. Under the steady-state conditions considered in the present work, equation (1)

uncouples from the solid displacement, and becomes a Poisson equation for the pressure field; i.e. one way-coupling.

In order to model the evolution of large-scale macroscopic cracks or fractures, as defined by discontinuities in the problem domain and described in terms of the stress intensity factor at the crack tip singularity, the two-way coupling of the transient poro-elasticity is essential. In this case, as the crack grows, the problem domain is continually changing in shape, with corresponding changes in the flow pattern, and therefore it is not possible to predict the final state of the crack evolution without considering the full transient problem. However, in this work we are interested in the steady state evolution of micro-cracks, which are defined by a continuous material damage formulation (see below). As described in the literature (e.g. [28]), this evolution may be defined in terms of a continuous nonlinear-elastic medium governed by a steady nonlinear Navier equation, which is a function of the damage parameter. The global evolution of the material damage occurs due to the formation of multiple micro-cracks and micro-fissures which weaken the porous medium, and the concurrent changes in permeability are considered without looking at the detail of how the cracks themselves are propagated on the micro-scale. The steady-state poroelastic equation is therefore used in the present work, with the corresponding one-way coupling between the Darcy equation and elasticity.

3 Material Damage due to the Evolution of Microcracks under Pressurised Flow Conditions

The injection of a pressurised fluid into the rock can lead to the development micro fractures, and/or force existing macro or micro cracks to further open. The propagation these fractures within a rock layer will result in an increase of the rock permeability, allowing faster migration of the flow through the rock formation. Even when a total failure of the rock does not occur, an increase in the length of cracks results in larger values of the effective rock permeability, with an associated increase in the rate of leakage for a given imposed pressure gradient.

Damage processes result in the development of surface discontinuities, in the form of microcracks and/or volume discontinuities as microvoids, which are generally both present. At the scale of microcracks the damage phenomenon results in a discontinuous medium. On the macroscale however, damage can be modelled via variables applicable to a continuum region [15]. In contrast to continuum damage phenomena, the fracture process is localized at the crack tip and gives rise to discontinuous fields for the displacement, traction and pore pressure variables.

We now suppose that the material is susceptible to stress-induced isotropic damage, which leads to an irreversible alteration in its poroelastic properties. In the isotropic damage model applied in [28], a scalar damage variable D is considered, such that $0 \leq D \leq D_c < 1$. When $D = 0$, the material has not been affected by damage. As D approaches the critical value D_C, the linear elasticity model is no longer valid and rupture can be expected. In a geomaterial that experiences isotropic damage, the net stress tensor σ_{ij}^n is related to the stress tensor σ_{ij} in the undamaged state by

$$\sigma_{ij}^n = \frac{\sigma_{ij}}{(1-D)} \tag{8}$$

The deformability parameters applicable to an initially isotropic elastic material, which experiences isotropic damage, can be updated by adjusting the linear elastic shear modulus by its equivalent that

is applicable to the damaged state, i.e.

$$\mu_d = (1 - D)\,\mu \tag{9}$$

with a corresponding expression for the effective stress tensor

$$\widetilde{\sigma}_{ij} = \lambda \varepsilon_{kk} \delta_{ij} + 2\mu_d \varepsilon_{ij} \tag{10}$$

The isotropic damage criteria governing the evolution of elastic stiffness and permeability parameters can be characterised by the dependency of damage variables on the distortional strain invariant. The damage model can be applied to examine the extent to which the poroelastic behaviour of saturated geomaterials can be influenced by the evolution of damage in the porous skeleton. An isotropic damage evolution law is employed in the analysis, which is characterised by the dependency of damage parameters on distortional strain invariants.

Following observation of experiments conducted on rocks, [19] propose that damage is a function of the shear strain energy and suggest the following damage evolution equation for rocks:

$$\frac{dD}{d\xi_d} = \gamma_1 \frac{\gamma_2 \xi_d}{(1 + \xi_d)} \left(1 - \frac{D}{D_c}\right) \tag{11}$$

where γ_1 and γ_2 are positive material constants, and the equivalent shear strain ξ_d is defined as

$$\xi_d = (e_{ij} e_{ij})^{\frac{1}{2}} \tag{12}$$

with

$$e_{ij} = \varepsilon_{ij} - \frac{1}{\delta_{ll}} \varepsilon_{kk} \delta_{ij} \tag{13}$$

Equation (11) can be integrated between an initial damage D_0 and D, which gives the expression for material damage as:

$$D = D_c - (D_c - D_0)\,(1 + \gamma_2 \xi_d)^{\frac{\gamma_1}{\gamma_2 D_c}}\, e^{-\frac{\gamma_1 \xi_d}{D_c}} \tag{14}$$

γ_1 and γ_2 are material-specific parameters describing the rate at which damage occurs within the poroelastic skeleton. These two parameters must be estimated experimentally for different materials.

Additionally a second criterion will be considered, based on the assumption that damage can only grow where the material deformations are dilatational. Thus, the equation (14) will only be applied at the locations where the first invariant of the strain tensor is positive, i.e., where

$$tr\,(\varepsilon_{ij}) > 0 \tag{15}$$

Consequently the damage function is variable in space, and as such, a localised evolution of damage can be expected.

Besides the reduction in the elastic shear modulus by the damage, the evolution of microcracks alters the permeability of the porous medium. Experimental observation in sandstone rocks by Shiping et al. (1994) suggest that, in the damaged state, the hydraulic conductivity can have quadratic variation with respect to equivalent shear strain ξ_d, given by

$$k_d = \left(1 + \beta \xi_d^2\right) k \tag{16}$$

where β is another experimentally determined material parameter.

As can be observed, in this type of formulation the damage and permeability are variable in space, and the resulting governing equation for the material deformation becomes nonlinear - even though it is based on the linear elasticity formulation - since the shear modulus is function of the damage and the damage is complex function of the shear stress. Finally, the definition of problem is completed by applying the corresponding boundary conditions for the flow velocity u_i and/or the pressure p. In the case of the elasticity equation, two types of boundary conditions are considered: Prescribed displacement $u_i = U_i$ (Dirichlet condition), and prescribed surface traction $\sigma_{ij} n_j = \tau_i$ (Neumann condition).

4 RBF-FC Method for Poroelasticity

A radial basis function depends upon the separation distances of a set of functional centres, and exhibits spherical symmetry around these centres. There are several commonly used radial basis functions (see [29]), however in this work we use the multiquadric RBF throughout (equation (17)), with $m = 1$.

$$\Psi(r) = \left(r^2 + c^2\right)^{\frac{m}{2}} \quad m \in \mathbb{Z}^+ \tag{17}$$

The c term, known as the shape parameter, describes the relative width of the RBF functions about their centres. Since c is a lengthscale it is appropriate to consider a non-dimensional alternative, $c^* = {}^{c}/_{\Delta}$, where Δ is typically related to the node separation distance in some way. The value of the shape parameter can have a dramatic effect on solution quality of RBF collocation methods, however for the proposed RBF-FC method the accuracy of the resulting solution is reasonably invariant of the shape parameter for sufficiently flat basis functions (i.e. sufficiently large values of c); see [12] for more detail.

The RBF-FC approach is a localised decomposition of the full-domain RBF collocation method for the solution of PDEs. The RBF collocation that is performed over each of the local stencils in the RBF-FC method is identical to the formulation for full-domain RBF collocation. Therefore, we first outline the full-domain RBF method for linear boundary value problems, before describing the decomposition used to form the RBF-FC method itself.

The full-domain Kansa RBF collocation method, [1],[2], constructs the continuous solution $u(x)$ of the PDE from a distinct set of N quasi-randomly distributed functional centres ξ_j:

$$u(x) = \sum_{j=1}^{N} \alpha_j \Psi\left(\|x - \xi_j\|\right) + \sum_{j=1}^{NP} \alpha_{j+N} P_{m-1}^{j}(x) \quad x \in \mathbb{R}^n \tag{18}$$

Here P_{m-1}^{j} is the j^{th} term of an order $(m-1)$ polynomial, under the constraint

$$\sum_{j=1}^{N} \alpha_j P_{m-1}^{k}(x_j) = 0 \quad k = 1, \ldots, NP \tag{19}$$

with NP being the total number of terms in the polynomial (determined by the polynomial order and the number of spatial dimensions). We consider a typical linear boundary value problem

$$\begin{aligned} L[u] &= f(x) \quad on\, \Omega \\ B[u] &= g(x) \quad on\, \partial\Omega \end{aligned} \tag{20}$$

where the operators $L[]$ and $B[]$ are linear partial differential operators on the domain Ω and on the boundary $\partial\Omega$, describing the governing equation and boundary conditions respectively. Collocating the interpolation formula (18) at N distinct locations known as test points, x_j , coinciding with the trial centres ξ_j, leads to a system of equations

$$\begin{bmatrix} B[\Psi] & B[P_{m-1}] \\ L[\Psi] & L[P_{m-1}] \\ P_{m-1} & 0 \end{bmatrix} \alpha = \begin{bmatrix} g \\ f \\ 0 \end{bmatrix} \tag{21}$$

which is fully populated and non-symmetric. In principle the set of functional centres ξ_i need not coincide with the set of test points x_i; however, in the present work the two sets are always of equal size and are placed at identical locations, leading to a single set of "collocation centres". In this way, the collocation matrix obtained is always a square system, and the resulting collocation system (21) may be solved directly, without recourse to least-square methods. This collocation approach is used to solve the pressure part of the poroelastic equation (1).

For coupled multivariate PDEs the basic RBF collocation formula (18) must be modified slightly. The following describes the formulation to solve the linear elasticity part of the poroelastic equation (7).

The Lamé-Navier equations for linear elastic deformation in terms of displacement, u_i, are given by

$$(\lambda + \mu) \frac{\partial^2 u_j}{\partial x_i \partial x_j} + \mu \frac{\partial^2 u_i}{\partial x_j^2} = -\rho b_i \tag{22}$$

for a body force b_i and material density ρ. In the poroelasticity model considered here, the effective body-force term, $-\rho b_i$, is given by the gradient of the pressure-field multiplied by the Biot number, i.e. $\alpha \frac{\partial p}{\partial x_i}$; see equation (7). In the case that material damage is considered, the elastic shear modulus, μ, is replaced by the equivalent shear modulus in the damaged material, $\overline{\mu}$; see equation (9).

Boundary conditions are applied either as a fixed displacement (Dirichlet condition), i.e.,

$$u_i = f_i \tag{23}$$

or as a prescribed surface traction (Neumann condition). The surface-traction operator at a surface with unit outward normal n_i and an applied traction g_i, is given by:

$$\lambda n_i \frac{\partial u_k}{\partial x_k} + \mu n_j \left(\frac{\partial u_i}{\partial x_j} + \frac{\partial u_j}{\partial x_i} \right) = \tau_i \tag{24}$$

Since the basis functions for Kansa's method are independent of the PDE being solved, the solution construction for Kansa's method is very similar to that of the single-variable formulation:

$$u_i(x) = \sum_{j=1}^{N} \alpha_{i,j} \Psi(\|x - \xi_j\|) + \sum_{j=1}^{NP} \alpha_{i,j+N} P_{m-1}^{j}(x), \quad i = 1, 2, 3 \tag{25}$$

Each variable u_i is constructed using a common set of RBF functional centres ξ_j, and the associated RBF weighting function α_i, for $i = 1, 2, 3$. The collocation system is generated by enforcing each component of the governing equation (22) at centres internal to the domain. The displacement (23) and surface-traction (24) operators are enforced at the appropriate centres on the domain boundary. In this way the set of test locations x_i is equal to the set of functional centres ξ_i. Subject to appropriate ordering, the resulting collocation system may be expressed as follows (excluding the polynomial terms for brevity):

$$\left[\begin{array}{ccc} \psi & 0 & 0 \\ B_{11}[\psi] & B_{12}[\psi] & B_{13}[\psi] \\ L_{11}[\psi] & L_{12}[\psi] & L_{13}[\psi] \\ \hline 0 & \psi & 0 \\ B_{21}[\psi] & B_{22}[\psi] & B_{23}[\psi] \\ L_{21}[\psi] & L_{22}[\psi] & L_{23}[\psi] \\ \hline 0 & 0 & \psi \\ B_{31}[\psi] & B_{32}[\psi] & B_{33}[\psi] \\ L_{31}[\psi] & L_{32}[\psi] & L_{33}[\psi] \end{array}\right] \left[\begin{array}{c} \\ \alpha_1 \\ \\ \hline \\ \alpha_2 \\ \\ \hline \\ \alpha_3 \\ \end{array}\right] = \left[\begin{array}{c} f_1 \\ \tau_1 \\ -\rho b_1 \\ \hline f_2 \\ \tau_2 \\ -\rho b_2 \\ \hline f_3 \\ \tau_3 \\ -\rho b_3 \end{array}\right] \tag{26}$$

The operators L_{ij} and B_{ij} represent the differential operators applied to u_j within the i^{th} equation of the PDE governing operator L and the surface traction operator B_N respectively. The functions L_{ij} and B_{ij} may therefore be expressed as:

$$L_{ij} = \mu\delta_{ij}\frac{\partial^2}{\partial x_k^2} + (\lambda+\mu)\frac{\partial^2}{\partial x_i \partial x_j} \qquad i,j = 1,2,3 \tag{27}$$

$$B_{ij} = \lambda n_i \frac{\partial}{\partial x_j} + \mu n_j \frac{\partial}{\partial x_i} + \mu\delta_{ij} n_k \frac{\partial}{\partial x_k} \qquad i,j = 1,2,3 \tag{28}$$

An equivalent operator for the Dirichlet boundary condition would be expressed as $B_{ij} = \delta_{ij}$.

The collocation matrix (26) represents a square and near-fully-populated linear system. When polynomial terms are included it is of size $n(N + NP) \times n(N + NP)$, where n is the number of spatial dimensions, N is the number of collocation points, and NP is the number of terms in the polynomial. To extend the collocation matrix to include the polynomial terms it is necessary to include them in the substitution of equation (25) into the governing and boundary operators (22), (23) and (24).

The RBF-FC solution procedure begins with a quasi-scattered set of nodes distributed over the interior of the domain, and over the domain boundaries. Around each internal node a local stencil is formed, which connects the node to its neighbours in some suitable fashion. The node around which the stencil is formed is identified as the centrepoint for that stencil, and of the resulting local RBF collocation system.

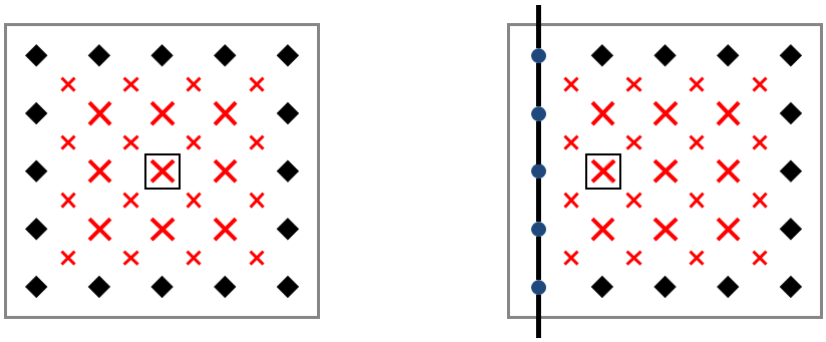

(a) Typical stencil; comprising strictly interior nodes

(b) Typical stencil; adjacent to domain boundary

Figure 1: Typical collocation stencil for the RBF-FC approach.
- Black marks represent collocation of the unknown solution value (solution centres).
- Blue circles represent collocation of the PDE boundary operator, where present (boundary centres)
- Red crosses represent collocation of the PDE governing operator (PDE centres).
- Smaller red crosses represent auxiliary PDE centres; additional locations at which the PDE governing operator is enforced locally (optional).
- Black square indicates the system centrepoint; the location around which the stencil is formed, and at which the global assembly is performed

The local RBF collocation systems take a form that aims to closely resemble their full-domain counterparts; each system collocates the unknown solution value around the periphery of its local domain (solution centres), and collocates the PDE governing operator throughout its interior (PDE centres); see Figure 1a. In this way the stencils act as local boundary value collocation systems, having Dirichlet boundaries of unknown value. Additional PDE centres may be placed at auxiliary locations within the stencil, not coincident with the global distribution of nodes. The addition of these auxiliary PDE centres can dramatically improve solution quality (see [12]), without increasing the number of unknowns present in the resulting sparse global assembly.

In the case that the stencil intersects with a domain boundary, the unknown Dirichlet boundary operator is replaced by the (known) domain boundary operator over the appropriate part of the stencil periphery, forming boundary centres (see Figure 1a). To maintain RBF system size, and therefore convergence rates, stencils which intersect the boundary are translated further into the domain, rather than being truncated.

Referring back to the original discretisation of the domain in terms of a set of quasi-scattered nodes; it is important to note that the operator applied at any given node will typically change between collocation systems. For example, a node placed within the interior of the domain can be expected to exist as a solution centre in some systems (where it is present on the periphery of the associated local stencil), and as a PDE centre in others (where it is interior to the local stencil). Nodes that are placed on the boundary of the domain, however, do not change context; they remain boundary centres for each system that they appear in.

By describing the stencils for the interpolation systems in this way, the meshless character of the RBF collocation approach is largely maintained. The collocation systems are defined as a collection

of nodes, which may be irregularly distributed, and are not subject to the volumetric constraints of element-based approaches; for example, it is not necessary to form a volumetric structure composed of edges and faces. Moreover, there is no issue of element inversion or other issues related to maintaining a good volumetric representation of the interpolation systems. As with all local approaches, some internal book-keeping is required; specifically, for each internal node it is necessary to define a list of other nodes that are connected to it, the differential operator to be applied at each connected node, and also the location of any auxiliary PDE centres. For static datasets this is purely a pre-processing issue, but in the case of a dynamic dataset some local stencil reconfiguration may periodically be required.

By forming an RBF collocation over each of the N stencils, which are formed around each strictly-interior domain node, a series of N RBF local collocation systems are formed:

$$A^{(k)}\alpha^{(k)} = d^{(k)} \qquad k = 1, ..., N \tag{29}$$

Here $A^{(k)}$ represents the collocation matrix for system k, and will be composed as described by equation (21), or equation (26), depending on whether the collocation is being performed for the pressure equation (1) or the elasticity equation (7). Similarly, $\alpha^{(k)}$ and $d^{(k)}$ are the interpolation coefficients and data vectors, respectively, for system k. The data vector $d^{(k)}$ contains the known boundary and PDE operator values, and also the unknown value of the solution field at the solution centres. As indicated in Figure 1, these solution centres lie on the periphery of the local system domain, and act as a local Dirichlet boundary condition for collocation system k.

Using the appropriate RBF reconstruction formula, i.e. equation (18), or equation (25), the approximate value of the field variable $u(x)$ (or a component thereof in the case of elasticity) may be computed for any x within the support domain of system k. Expressing this computation as a vector product we have

$$u^{(k)}(x) = H^{(k)}(x)\,\alpha^{(k)} \tag{30}$$

where $H^{(k)}(x)$ is identified as a reconstruction vector for system k at location x.

By reconstructing the value of u at the system centrepoint, $x_c^{(k)}$; i.e. the node around which the stencil for system k was originally formed, we obtain:

$$\begin{aligned} u^{(k)}\left(x_c^{(k)}\right) &= H^{(k)}\left(x_c^{(k)}\right)\alpha^{(k)} \\ &= H^{(k)}\left(x_c^{(k)}\right)\left[A^{(k)}\right]^{-1} d^{(k)} \\ &= W^{(k)}\left(x_c^{(k)}\right) d^{(k)} \end{aligned} \tag{31}$$

Here $W^{(k)}(x_c) = H^{(k)}(x_c)\left[A^{(k)}\right]^{-1}$ is a stencil weights vector, expressing the value of the solution field u, at the system centrepoint $x_c^{(k)}$, in terms of the entries in the data vector $d^{(k)}$. This value of u at $x_c^{(k)}$, as reconstructed by equation (31), will appear as an unknown within the data vector for any systems which have within their stencil a solution centre located at $x_c^{(k)}$; i.e. any systems which have this node on their periphery. Therefore, by performing the above reconstruction (31) at the centrepoint of each local system k, a series of N simultaneous equations are formed for the N unknown values of $u^{(k)}$ at the system centrepoints. Solution of this sparse global system therefore yields the value of u at each of the N internal nodes. By feeding these values back into the local data vectors, $d^{(k)}$, the local

systems may be used to extract any other field values as may be required for post-process analysis (such as pressure gradients or stresses).

Note that the weights vectors may be obtained by solving the linear system

$$\left[A^{(k)}\right]^T W^{(k)} \left(x_c\right)^T = H^{(k)} \left(x_c\right)^T \tag{32}$$

thereby avoiding the need to explicitly compute the matrix inverse $\left[A^{(k)}\right]^{-1}$

In the sparse global system the PDE governing operator and the corresponding boundary conditions of the problem have already been imposed within the local collocation systems. The number of non-zero matrix entries in each row corresponds to the number of solution centres in the associated local system; i.e. the number of nodes on the stencil periphery. In this way the number of non-zero entries in each row of the global assembly does not increase as the size of the dataset grows. With an appropriate sparse linear system solver the method may be scaled efficiently to very large datasets, so long as the local stencil size remains constant. The numerical results presented in Section 5 demonstrate that high convergence rates and extremely accurate solutions may be obtained in this way, using stencils of fixed size (i.e. a pre-defined number of collocation centres and resulting matrix bandwidth).

The solution procedure for the proposed RBF-FC method may therefore be summarised as follows:

1. Generate a set of nodes to adequately discretise the boundary and the interior of the solution domain.

2. Around each interior node, form a local stencil by connecting the node to its neighbours in some appropriate fashion. The node around which the stencil is formed is identified as the 'centrepoint' for this stencil.

3. Form an RBF collocation over each stencil, subject to the following guidelines:

   - At nodes interior to the stencil, including the centrepoint itself, collocate the governing PDE operator (thereby forming PDE centres).
   - At nodes on the stencil periphery, collocate the Dirichlet operator with an unknown value (thereby forming solution centres).
   - If the stencil intersects the domain boundary, replace the solution centres with collocation of the appropriate domain boundary condition (thereby forming boundary centres).
   - Auxiliary PDE centres may optionally be included, at locations not coinciding with the nodes. These auxiliary PDE centres are used to improve the accuracy of the local boundary value problems, without increasing the number of unknowns in the global assembly.

4. For each local collocation system, form a reconstruction vector for the Dirichlet solution value at the system centrepoint, and solve equation (32) in order to obtain a "weights vector". This weights vector describes the value of the solution at the system centrepoint in terms of its value at the solution centres of the local system. This typically represents the most computationally expensive stage of the procedure.

5. Assemble the weights vectors for each of the local systems, forming a sparse global system. The number of non-zero entries in each row (i.e. matrix bandwidth) is equal to the number of solution centres in the associated local system.

6. Solve the sparse global assembly, thereby obtaining the value of the solution field at each interior node

7. Place the obtained values of the solution field into the local system right-hand-side vectors, to allow reconstruction of any other required data-fields (such as stresses or other partial derivatives) throughout the domain.

The poroelastic solution procedure first solves the Darcy pressure equation (1), obtaining the pressure-field, p, at every node within the domain, then reconstructs the pressure gradients $\frac{\partial p}{\partial x_i}$ at each PDE centre (including any auxiliary PDE centres). The solution of the Darcy equation takes place as described above for a generalised scalar problem; see equation (20). In this instance the governing PDE operator is given by

$$L = \frac{\partial}{\partial x_i}\left(k_{ij}\frac{\partial}{\partial x_j}\right) \tag{33}$$

The boundary operators will be of either Dirichlet, Neumann or Robin operator type, depending on the requirements of the problem.

To obtain the pressure gradients, first note that any derivative of the field variable u in the RBF approximation (18) may be obtained by applying the appropriate differential operator to the radial basis functions themselves. Since the radial basis functions, ψ, are known; see equation (17), their derivatives may be computed analytically. For a general partial differential operator Q, the equivalent RBF reconstruction formula (18) would become:

$$Q\left[u\left(x\right)\right] = \sum_{j=1}^{N} \alpha_j Q\left[\Psi\left(\left\|x-\xi_j\right\|\right)\right] + \sum_{j=1}^{NP} \alpha_{j+N} Q\left[P_{m-1}^{j}\left(x\right)\right] \quad x \in \mathbb{R}^n \tag{34}$$

Writing the above as a vector product, performed at the collocation stencil k, we obtain

$$Q\left[u^{(k)}\left(x\right)\right] = H_Q^{(k)}\left(x\right)\,\alpha^{(k)} \tag{35}$$

where $H_Q^{(k)}\left(x\right)$ is identified as a reconstruction vector for the differential operator Q, using the local system k, at x. A solution weights vector for differential operator Q may then be obtained; i.e. $W_Q^{(k)}\left(x_c\right) = H_Q^{(k)}\left(x_c\right)\left[A^{(k)}\right]^{-1}$, and the desired value of the differential operator applied to the field variable may then be obtained; i.e.

$$Q\left[u^{(k)}\left(x\right)\right] = W_Q^{(k)}\left(x\right)\,d^{(k)} \tag{36}$$

for any x within the domain of system k. Note that the local data vector, $d^{(k)}$, will now contain the values of the field variable (i.e. the recently computed nodal pressure values), and so is at this stage completely known. The value of the differential operator is therefore be obtained directly, without recourse to forming a further sparse global assembly. For the reconstruction of pressure gradients, the general partial differential operator, Q, is be given by

$$Q_i^{grad} = \frac{\partial}{\partial x_i} \tag{37}$$

The pressure gradients are then used to determine the inhomogeneous term of the elasticity equation (7), which is solved using the RBF-FC procedure. The resulting stress fields can then be obtained via reconstruction, as outlined above, with the reconstruction operator Q as defined by the stress-strain relationship (2).

In the case of a material damage analysis, the resulting stress fields are then used to determine the damage variable D at each node; see equation (11). The damage variable, along with the material parameters γ_1, γ_2 and β, can then be used to obtain the damaged shear modulus μ_d; see (9), and the damaged hydraulic conductivity k_d; see (16). These damaged variables are used within the poroelasticity PDE that is solved in the following iteration, and the iterative procedure continues until convergence is attained.

5 Numerical Results

As described in Section 4, the proposed solution procedure for the poroelastic equation involves first solving the Darcy equation to obtain the pressure field and pressure gradients, and then solving an inhomogeneous linear elasticity equation to obtain the resulting stress and displacement fields. The RBF-FC method has, in [12], been validated for the solution of general convection-diffusion diffusion equations, showing the ability to solve strongly convective PDEs on centrally defined stencils (the "implicit upwinding" effect of the RBF-FC method). In the same work the solution of the homogeneous linear elasticity equation was also investigated, and for investigated both PDEs the method was shown to exhibit high convergence rates - in excess of sixth order - and a high stability to variations in the value of the RBF shape parameter, c; see equation (17). The numerical examples presented here investigate the performance of the method for the solution of the steady poroelastic equation, and for the prediction of material damage.

To verify the proposed numerical method we formulate an analytical solution for a poroelastic injection scenario, as a cylindrical annulus under a fixed internal and external pressure. This analytical solution is used to explore the solution accuracy and rate of convergence for Darcy flow, and for the full poroelastic expression, by considering the injection of water into sandstone. Finally we carry out a simple analysis of hydromechanical damage for this injection scenario, using material damage parameters obtained from the literature. Here we vary the pressure of injection to examine the accumulation of damage within the material, we compute the critical pressure at which the material breaks down, and we investigate the benefits of injecting a given volumetric flux into a medium which has been pre-damaged, in comparison to injection into an undamaged medium.

Poroelastic annulus at fixed internal and external pressure

We examine a porous cylindrical annulus subject to a large internal pressure, formulating an analytical solution for this scenario to allow numerical verification. For a cylindrical annulus with inner radius a and outer radius b, with pressure p_1 at $r = a$ (i.e. internal pressure) and pressure p_0 at $r = b$ (i.e. external pressure), the pressure field is given by:

$$p = \frac{p_0 - p_1}{\ln\left(b/a\right)} \ln\left(r\right) + \frac{p_1 \ln\left(b\right) - p_0 \ln\left(a\right)}{\ln\left(b/a\right)} \tag{38}$$

The analytical solution for the displacement and stress fields is then obtained as:

$$\begin{aligned} u_r(r) &= Ar + Br^{-1} + \xi_1\left(\frac{r}{2}\ln(r) - \frac{r}{4}\right) + \xi_2\frac{r}{2} \\ \sigma_{rr} &= (\lambda+\mu)\left[2A + \xi_1\ln(r) + \xi_2\right] - 2\mu Br^{-2} + \frac{\xi_1\mu}{2} - \alpha p \\ \sigma_{\theta\theta} &= (\lambda+\mu)\left[2A + \xi_1\ln(r) + \xi_2\right] + 2\mu Br^{-2} - \frac{\xi_1\mu}{2} - \alpha p \\ \sigma_{r\theta} &= 0 \end{aligned} \tag{39}$$

where

$$\begin{aligned} A &= \frac{1}{2(\lambda+\mu)}\left[\frac{p_1a^2 - p_0b^2}{b^2-a^2}\left(1 - \frac{\alpha\mu}{\lambda+2\mu}\right) + \frac{\alpha\mu(p_1-p_0)}{2(\lambda+2\mu)\ln(b/a)}\right] \\ B &= \frac{a^2b^2(p_1-p_0)}{2\mu(b^2-a^2)}\left[1 - \frac{\alpha\mu}{\lambda+2\mu}\right] \\ \xi_1 &= \frac{\alpha(p_0-p_1)}{(\lambda+2\mu)\ln(b/a)} \\ \xi_2 &= \frac{\alpha(p_1\ln(b) - p_0\ln(a))}{(\lambda+2\mu)\ln(b/a)} \end{aligned} \tag{40}$$

Observe that, in the case of $\alpha = 0$, the poroelastic governing equation (7) is reduced to that of linear elasticity; i.e. it becomes decoupled from the pressure equation throughout the domain interior. In this scenario the above expression (39) is reduced to the well known analytical solution for a linear elastic cylindrical annulus under fixed internal and external pressure.

Taking an inner radius of $a = 2$m and an outer radius of $b = 10$m we exploit the symmetry of the problem and examine one quarter of the domain, imposing the appropriate pressure-traction boundary conditions at the inner and outer surface, and enforcing symmetry at the $x = 0$ and $y = 0$ boundaries; see Figure 2a. The problem is solved using Cartesian co-ordinates. We take a Young's modulus $E = 27.6GPa$, a Poisson ratio $\nu = 0.15$, hydraulic conductivity $k = 10^{-6}\mathrm{m\,s^{-1}}$, and the Biot number as $\alpha = 0.64$, representing Weber sandstone. Choosing the inner pressure as $p_1 = 100$MPa and the outer pressure as $p_0 = 10$MPa, the resulting stress-field is shown in Figure 2.

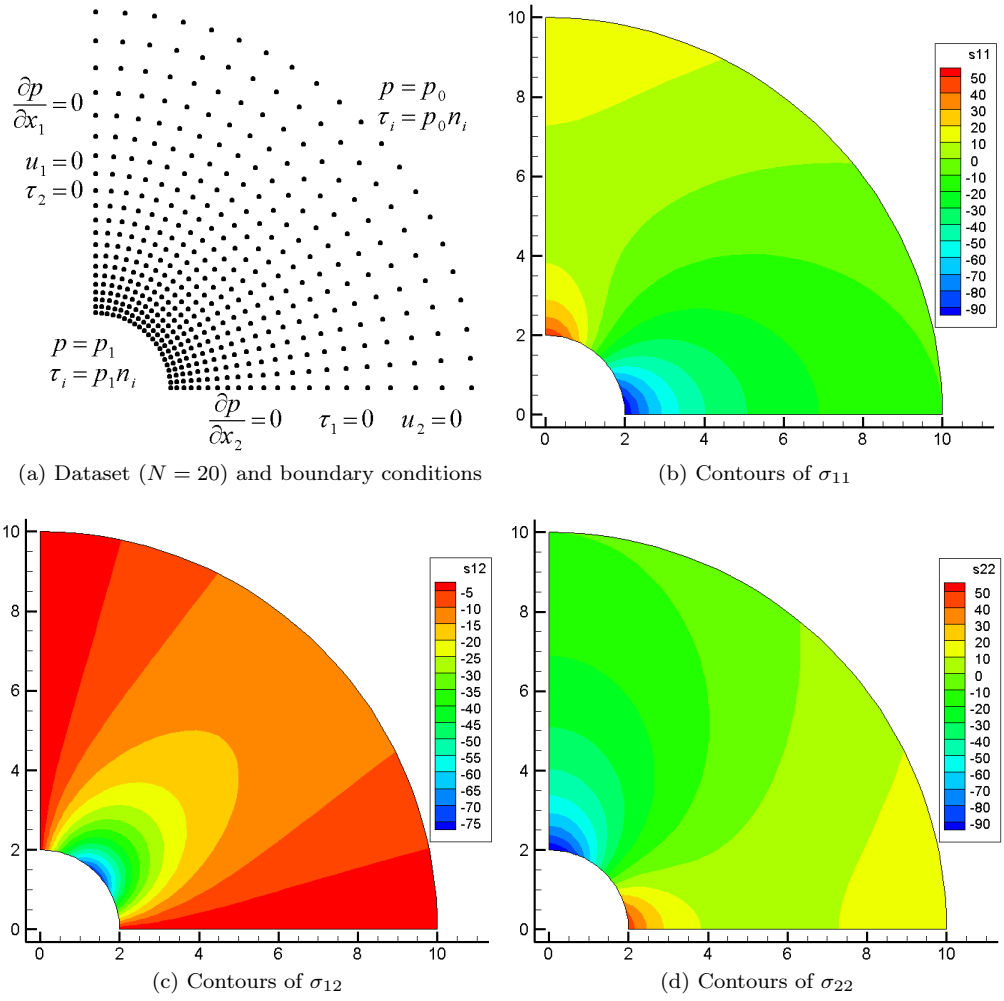

(a) Dataset ($N = 20$) and boundary conditions

(b) Contours of σ_{11}

(c) Contours of σ_{12}

(d) Contours of σ_{22}

Figure 2: Dataset, boundary conditions and stress-field representation

The solution domain is discretised with $(N+1)\times(N+1)$ nodes (see Figure 2a), and local stencils are formed by connecting together neighbouring nodes in order to form a 5×5 stencil, with auxiliary PDE centres placed at every Cartesian half-interval, as is represented by the sketch in Figure 1. A shape parameter of $c^* = 100$ is used, scaling against the minimum separation from the system centrepoint to its nearest neighbouring node. We examine datasets of size $N = 20$, 30, 40, 60, 80, recording in Table 1 the L_2 relative error observed for the displacement magnitude, and for each of the stress components. Note that, owing to symmetry, the errors for the σ_{22} stress component are identical to those of σ_{11} and are therefore omitted.

	p	$\left\lvert\frac{\partial p}{\partial x_i}\right\rvert$	$\lvert u_i \rvert$	σ_{11}	σ_{12}
$N = 20$	1.82×10^{-7}	2.81×10^{-7}	4.60×10^{-5}	2.48×10^{-5}	4.01×10^{-5}
$N = 30$	4.44×10^{-9}	7.08×10^{-9}	7.19×10^{-7}	6.12×10^{-7}	6.49×10^{-7}
$N = 40$	6.03×10^{-10}	9.60×10^{-10}	9.97×10^{-8}	7.53×10^{-8}	9.50×10^{-8}
$N = 60$	6.47×10^{-11}	1.04×10^{-10}	8.34×10^{-9}	4.65×10^{-9}	6.08×10^{-9}
$N = 80$	1.37×10^{-11}	2.26×10^{-11}	1.65×10^{-9}	7.01×10^{-10}	8.90×10^{-10}

Table 1: L_2 relative errors for: pressure, pressure gradient, displacement magnitude, stresses, at various dataset densities

The method exhibits highly accurate solutions; on the $N = 80$ dataset we observe L_2 relative errors of around 10^{-9} for the stress and displacement fields, and around 10^{-11} for the pressure and pressure gradient fields. In each case the errors arising from the solution of the Darcy equation for pressure are roughly two orders of magnitude smaller than those arising from the inhomogeneous linear elasticity equation for displacement. In each case the error observed from the gradient of the respective solution field (i.e. pressure gradient and stresses) is roughly equivalent to the error observed in the solution field itself (i.e. pressure and displacement). This ability to obtain highly accurate representations of field derivatives represents a powerful feature of the proposed numerical method. In many other numerical methods, such as finite volume and finite element methods, the error in the field derivatives can be expected to be substantially higher than the error observed in the field variables; often with a reduced rate of convergence.

The errors given in Table 1 are plotted in Figure 3, showing clear and consistent convergence for each data field. While the improved accuracy of the pressure and pressure-gradient fields is clearly visible in the plot, the rate of convergence (i.e. the gradient of the resulting curves) is very close to that of the displacement and stress fields. In each case a convergence rate of roughly seventh order is observed.

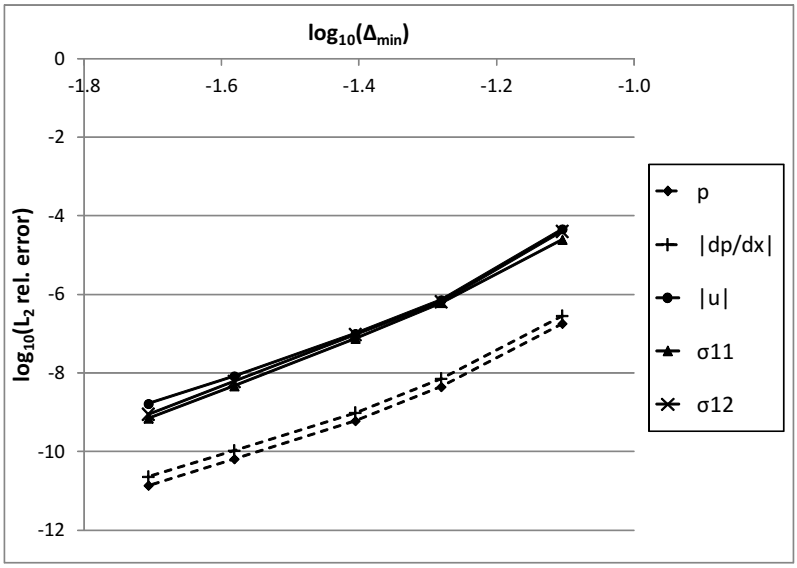

Figure 3: Spatial convergence: Poroelastic analytical cylinder under injection pressure

Hydromechanical damage during high-pressure fluid injection

We present now a preliminary investigation into the hydromechanical damage that may occur during a high-pressure injection of water into a sandstone. The investigation intends to highlight some of the general features that arise during such injection, and assess the impact of varying properties such as injection pressure, material stiffness, and the previously identified damage parameters. As described in Section 3, the hydromechanical damage process is a nonlinear problem, owing to the coupling between the hydromechanical damage, D, and the properties of the injected medium; i.e. damaged shear modulus, μ_d, and damaged hydraulic conductivity, k_d. In each case the nonlinear procedure progresses as a series of Picard iterations; using the most up to date values of μ_d and k_d, within the RBF-FC solution procedure, updating their values after each iteration. The iterative process is considered to have converged when the relative change in the predicted damage field, D, changes by a relative value of less than 10^{-5}. We note that, in most cases, this convergence is achieved after either five or six nonlinear iterations.

We take as baseline values the material properties from the previous numerical example; i.e. $E = 27.6GPa$, $\nu = 0.15$, $k_0 = 10^{-6}\mathrm{m\,s^{-1}}$, and $\alpha = 0.64$. Additionally, we take baseline values for the empirical damage parameters as $\gamma_1 = \gamma_2 = 130$, and $\beta = 3 \times 10^5$, as suggested for sandstone in the work of Selvadurai; see [28]. The initial damage to the material, D_0, is taken to be zero, and the critical damage parameter, D_c, which represents the damage at which the porous skeleton itself breaks down, is set as $D_c = 0.75$. Beyond this value the continuum damage model is no longer applicable and macroscopic fractures can be expected to dominate. Unless otherwise stated, the above values are used throughout this investigation.

The solution domain takes an inner radius of 2m, and an outer radius of 20m; twice the outer radius used in the previous numerical example. The domain is discretised by 31 nodes in the radial direction

and 21 nodes in the axial direction. At the $x = 0$ and $y = 0$ boundaries we enforce symmetry, and at the inner surface we enforce the pressure-traction boundary condition for the injection pressure p_0; i.e. $\tau_i = -p_0 n_i$. At the outer boundary we enforce a pressure and surface traction that represents the solution domain as being nested within a larger domain, of radius 50m. By evaluating the pressure at $r = 20$m, as given by equation (38) taking $b = 50$m and $p_1 = 0$, the outer pressure boundary condition is defined. Similarly, the surface traction is obtained by evaluating the analytical stress field given by equation (39), under the same assumptions, at $r = 20$m.

Figure 4a shows the material damage predicted using the above described parameters, with an injection pressure of $P_0 = 200$MPa (Figure 4a). The resulting increase in the hydraulic conductivity is given in Figure 4b. The material damage is largest in the region immediately around the injection site, and decays rapidly as the separation from the injection well increases. In this case a significant increase in hydraulic conductivity is observed, with the value of k at the injection well being roughly a factor of 45 larger than the undamaged hydraulic conductivity k_0. The radial variation of damage and hydraulic conductivity for this case is shown in Figure 5. Here the rapid decay of both damage and hydraulic conductivity can be clearly observed.

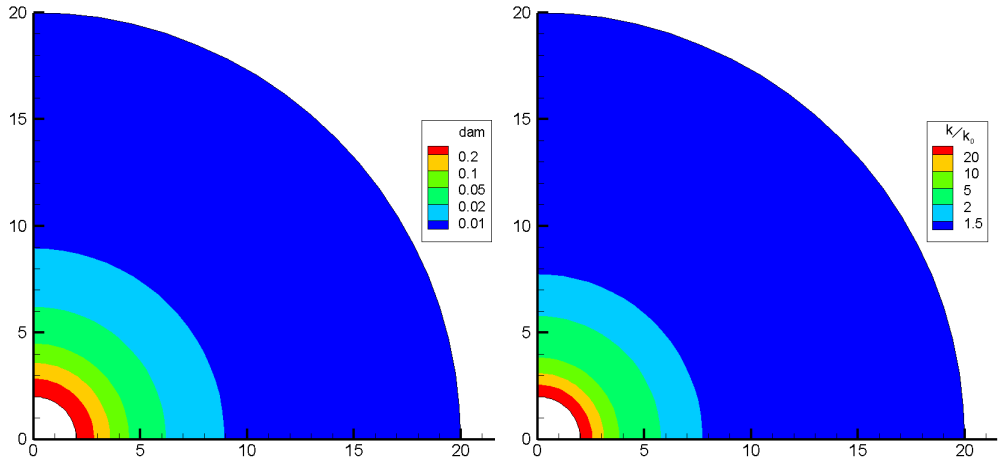

(a) Material damage (D) (b) Increase in hydraulic conductivity

Figure 4: Damage field and increase in hydraulic conductivity: $p_0 = 200$ m H_2O

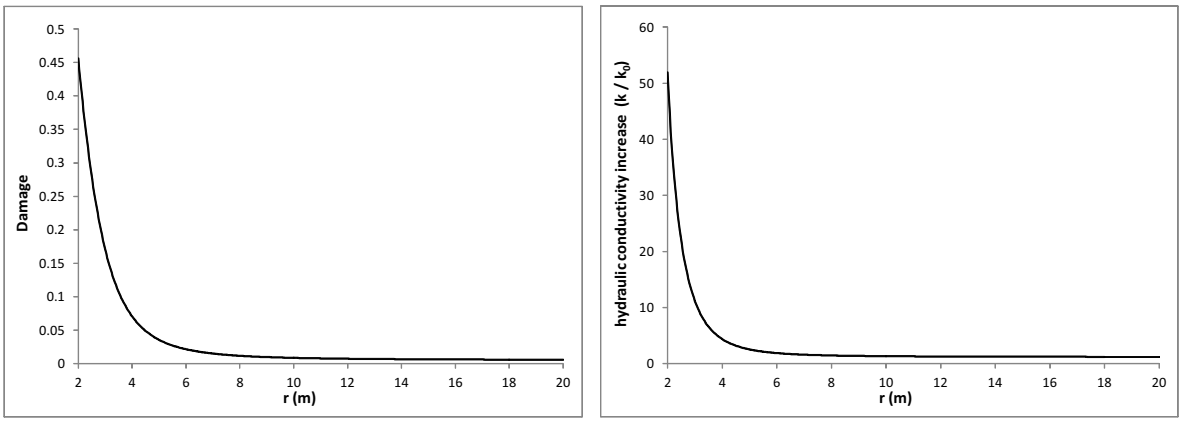

(a) Material damage (D) (b) Increase in hydraulic conductivity

Figure 5: Radial variation of damage and hydraulic conductivity: $p_0 = 200$ m H_2O

By varying the injection pressure, p_0, we may examine the propagation of damage through the domain. Figure 6a plots the volume of the domain over which the damage variable D is at least 2%, 5% and 10%, for injection pressures in the range 50MPa $< p_0 \leq$ 300MPa. Figure 6b shows the volume over which the hydraulic conductivity has increased by a factor of 2, a factor of 5 and a factor of 10. From these plots is is clear that the volume of damaged material increases dramatically with increased pressure; as does the volume of increased hydraulic conductivity. This is particularly true for small increases in damage ($D > 2\%$) and hydraulic conductivity ($k/k_0 > 2$); at high pressures a significant volume of material is affected to these thresholds or above.

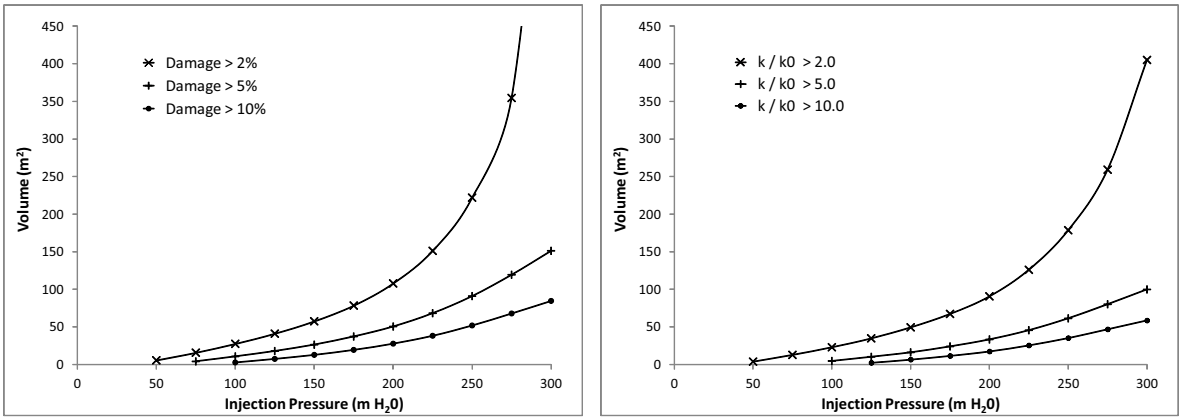

(a) Damage propagation (b) Increased hydraulic conductivity

Figure 6: Propagation of damage and increased hydraulic conductivity into the domain, for varying pressure

By further increasing p_0, we may estimate the injection pressure at which the critical damage, $D = D_c$, is first observed within the material. Here the critical injection pressure is found to be roughly $p_{crit} = 335$ m H_2O, and the critical damage occurs in the region immediately adjacent to the injection location; see Figure 7. At injection pressures above this critical value, the formation of macroscopic fractures can be expected to dominate (i.e. hydraulic fracturing). If the formation of macroscopic fractures within the material is desirable, as can be expected in the case of the hydraulic fracturing of shale to extract natural gas, then injection pressures above this critical value should be targeted. In the case of the geological sequestration of CO2, for example, maintaining the integrity of the porous medium is an important requirement to reduce the occurrence of leakage around the site of injection, and therefore injection pressures below the critical threshold should be targeted.

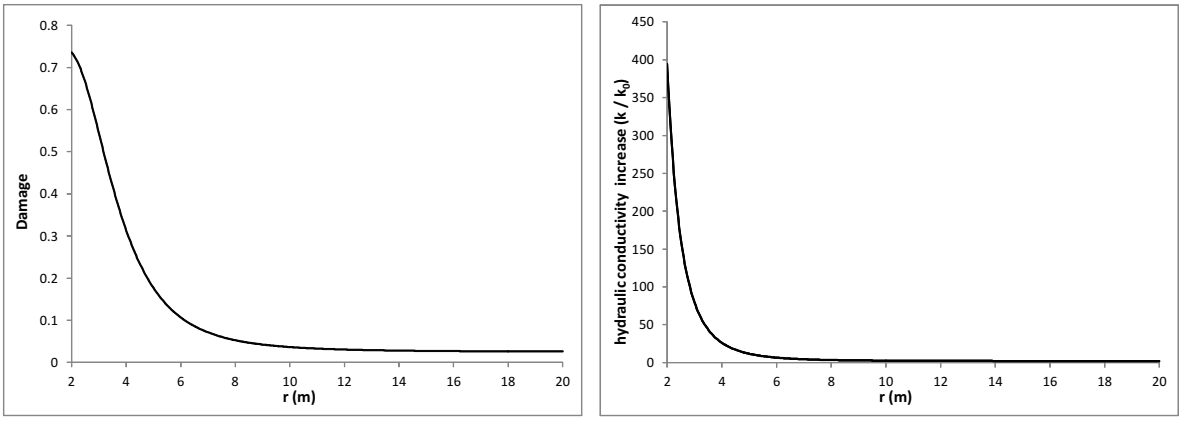

(a) Material damage (D)

(b) Increase in hydraulic conductivity

Figure 7: Radial variation of damage and hydraulic conductivity at critical injection pressure; $p_{crit} = 335\,\mathrm{m}\ H_2O$

It is important to note that the material damage described here is an irreversible process, and therefore it is possible to "pre-damage" the material using a high pressure injection of water, or other suitable fluid, before the injection of the intended storage fluid commences. In this way the material damage and associated increase in hydraulic conductivity can be achieved without recourse to high pressure injection in the long term. However, given the requirement to avoid the formation of macroscopic fractures around the injection site that may risk the integrity of the well, the injection pressure must be chosen carefully. The selection of a suitable injection pressure will therefore require a careful assessment of the material strength at the injection site, and also a careful assessment of the empirical parameters that appear in the damage formulation; i.e. γ_1 and γ_2.

By pre-damaging the injection site the resistance to the injected fluid is reduced, owing to the increased hydraulic conductivity in this region. In this way, the injection pressure required for the storage of a given mass flux can be reduced significantly, therefore reducing the energy expenditure required for continuous injection. Figure 8 shows the pressure fields predicted during an injection scenario, during which 0.5 $m^2\mathrm{h}r^{-1}$of fluid is injected at a constant rate throughout the surface of the pipe; i.e. imposing a volumetric flux of $k\frac{\partial p}{\partial r} = \frac{1}{8\pi}\mathrm{m\ h}r^{-1}$ in the radial direction at the inner surface (i.e. $r = a = 2\mathrm{m}$).

In Figure 8a the substrate is undamaged, having a constant hydraulic conductivity of $k_0 = 10^{-6}$m s^{-1}. In Figure 8b the substrate has been pre-damaged by injecting at a pressure of 200MPa, resulting in a hydraulic conductivity field as represented by Figures 4b and 5b. Injection into the pre-damaged substrate (Figure 8b) requires a significantly lower injection pressure; 33.98MPa, than does injecting into the undamaged substrate (Figure 8a), which requires $p_0 = 71.15$MPa for the same injection rate of 0.5 $m^2 \text{hr}^{-1}$. Note that this reduction in pressure required for injection into the damaged substrate, while significant, is not so large as may be expected from the factor of fifty increase in k that is observed at the surface of the pipe in this case (see Figure 5b). This is due to an associated reduction in radial pressure gradient close to the pipe surface, which is clearly visible by comparing the pressure contours of Figures 8a and 8b.

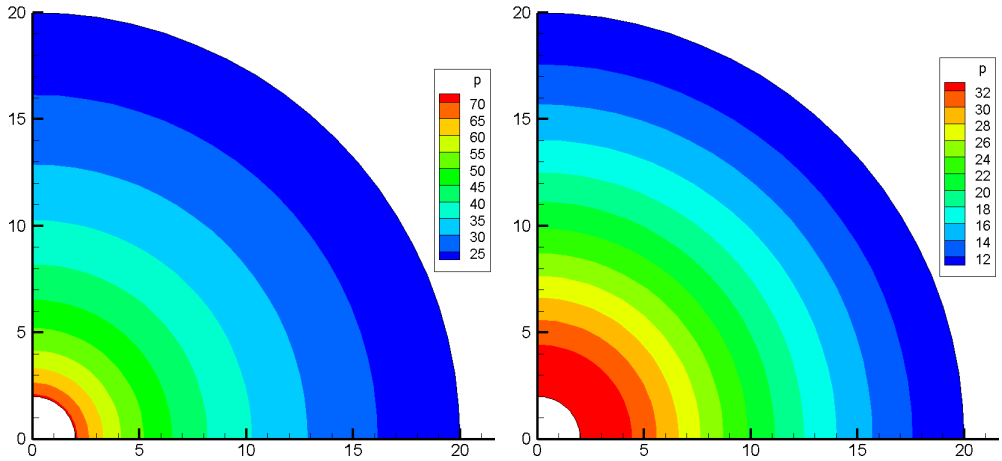

(a) Undamaged material

(b) Material pre-damaged by $p_0 = 200$MPa injection

Figure 8: Pressure fields associated with a fluid injection rate of 0.5 $m^2 \text{hr}^{-1}$ for injection into damaged and undamaged substrate

Figure 9 demonstrates the effect of varying the material strength under an injection pressure of $p_0 =$ 150 m H_2O. The plot shows the propagation of damage into the material for a Young's modulus of $E = 13.8GPa$ (Figure 9a); i.e. half the original value of E, and $E = 55.2GPa$ (Figure 9b); i.e. double the original value of E. As can be observed from the figure, the damage propagates significantly further into the weaker material, and a significantly higher maximum damage is observed.

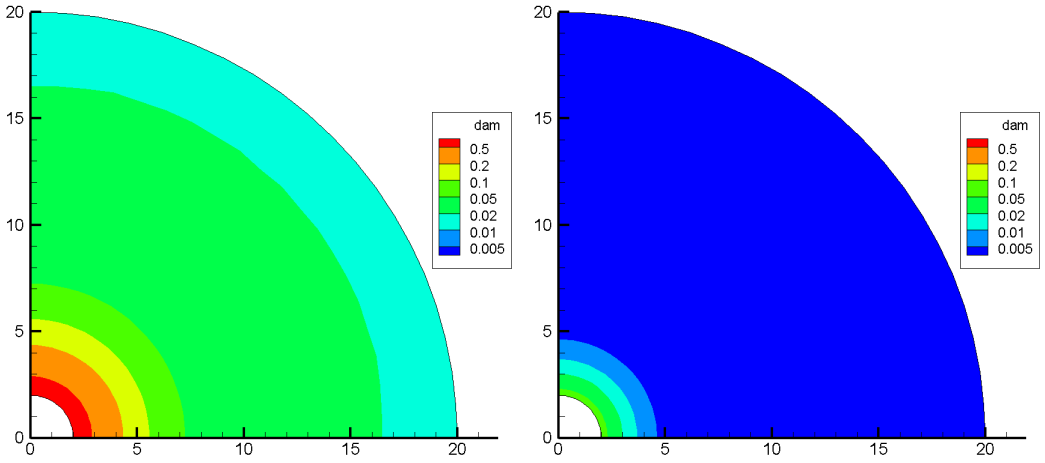

(a) $E = 13.8GPa$ (b) $E = 55.2GPa$

Figure 9: Material damage propagation at varying material stiffness; $p_0 = 150\,\text{m}$ H_2O

The resulting damage field is found to be significantly less sensitive to variations in the Poisson ratio than it is to variations in Young's modulus. Figure 10 shows the damage field predicted for $\nu = 0.1$ (Figure 10a), and $\nu = 0.3$ (Figure 10b), with an injection pressure of $p_0 = 100\,\text{m}$ H_2O. As can be observed from comparing the two plots, only a relatively minor variation in damage propagation is observed across this range of Poisson ratios. The larger Poisson ratio shows a slightly higher maximum damage, which propagates slightly further into the domain.

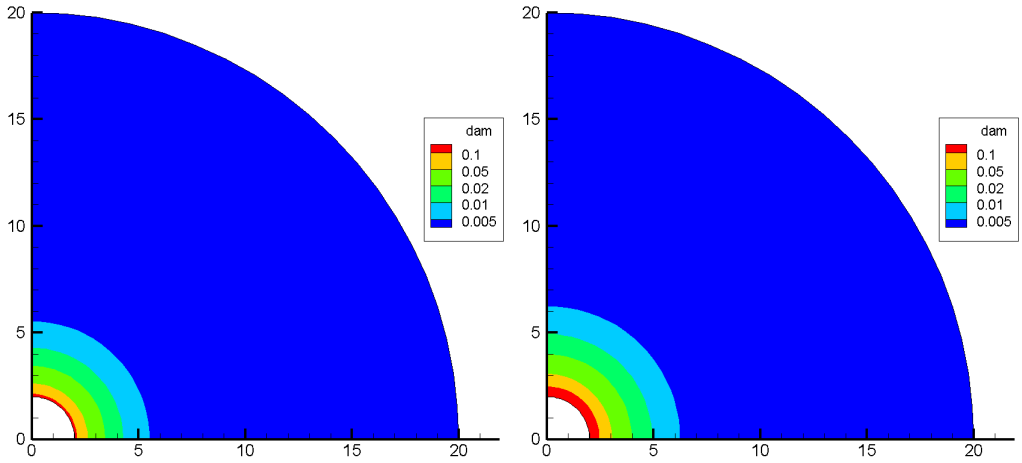

(a) $\nu = 0.1$ (b) $\nu = 0.3$

Figure 10: Material damage propagation at varying Poisson ratio; $p_0 = 150\,\text{m}$ H_2O

Given the observed sensitivity of the material damage to changes in material strength, and the potential difficulty of determining the empirically-derived damage parameters γ_1 and γ_2, it may be preferable in practice to progressively damage the material, rather than estimating the critical injection pressure, p_{crit}, a-priori. A relatively safe injection pressure may be selected, with the aim of producing minimal damage to the material. The increase in material damage at the injection site may then be investigated experimentally, allowing an improved estimate for an increased injection pressure. In this way the desired increase in hydraulic conductivity may be attained, with a reduced risk of exceeding the critical damage threshold (D_c) and damaging the integrity of the injection site.

6 Conclusions

In this work, a high-resolution scalable meshless numerical method is described for the solution of steady poroelastic problems. Based on a local collocation with radial basis functions, the proposed RBF finite collocation approach (RBF-FC) retains many of the desirable characteristics of full-domain RBF collocation methods; such as the ability to operate on irregular datasets and impose arbitrary boundary operators, without exhibiting the computational cost and numerical ill-conditioning issues associated with such full-domain collocation methods. The formulation of the method is described in detail for the solution of linear scalar problems, linear elasticity, and the steady poroelastic equation.

To verify the implementation of the RBF-FC for steady poroelastic analysis, an analytical solution is formulated for the pressurised injection of liquid into a porous medium. Comparison of numerical predictions with the analytical solution show that the method is capable of high accuracy, and exhibits convergence rates of roughly seventh order. The method is shown to be capable of obtaining the derivatives of field variables, such as pressure gradients and hydromechanical stresses, to the same level of accuracy as the field variables themselves (i.e. pressure and displacement).

The numerical method is applied to investigate the hydromechanical damage of a sandstone during high-pressure fluid injection. In this nonlinear problem the formation of micro-cracks and micro-fissures is estimated via a continuum damage parameter, which modifies the bulk shear modulus and hydraulic conductivity of the injected medium. The magnitude of material damage and the extent of its propagation into the medium is investigated by adjusting the injection pressure and material strength. It may be observed that, once the injection pressure is sufficiently large to cause appreciable damage to the porous medium, further increases in pressure will rapidly increase the amount of damage, and the radius at which it propagates into the domain. The formation of damage is strongly dependent on the Young's modulus of the substrate, yet only weakly dependent on the Poisson ratio. The formation of material damage in this scenario significantly increases the hydraulic conductivity of the medium in the region around the injection site, which in turn reduces the resistance of the material to the injected fluid.

References

[1] E. J. Kansa. Multiquadrics - a scattered data approximation scheme with applications to computational fluid-dynamics-i: Surface approximations and partial deriviatives estimates. *Comput. Math. Appl.*, 19:127–145, 1990.

[2] E. J. Kansa. Multiquadrics - a scattered data approximation scheme with applications to computational fluid dynamics-ii: Solution to parabolic, hyperbolic and elliptic partial differential equations. *Comput. Math. Appl.*, 19:147–161, 1990.

[3] Z. Wu. Compactly supported positive definite radial basis functions. *Adv. Comput. Math.*, 4:75–97, 1995.

[4] H. Wendland. Piecewise polynomial, positive definite and compactly supported radial basis functions of minimal degree. *Adv. Comput. Math.*, 4:389–396, 1995.

[5] H. Wendland. Error estimates for interpolation by compactly supported radial basis functions of minimal degree. *Journal of Approximation Theory*, 93:258–272, 1998.

[6] G.R Liu and Y.T Gu. A local radial point interpolation method (lrpim) for free vibration analyses of 2-d solids. *Journal of Sound and Vibration*, 246(1):29–46, 2001.

[7] B. Sarler and R. Vertnik. Meshless explicit local radial basis function collocation methods for diffusion problems. *Comput. Math. Appl.*, 51:1269–1282, 2006.

[8] G. Wright and B. Fornberg. Scattered node compact finite difference-type formulas generated from radial basis functions. *J. of Comput. Phys.*, 212:99–123, 2006.

[9] E. Divo and A. Kassab. An efficient localised radial basis function meshless method for fluid flow and conjugate heat transfer. *Journal of Heat Transfer*, 129:124–136, 2007.

[10] D. Stevens, H. Power, M. Lees, and H. Morvan. The use of PDE centres in the local RBF Hermitian method for 3D convective-diffusion problems. *J. Comput. Phys.*, 228:4606–4624, 2009.

[11] N Flyer, E Lehto, S Blaise, G.B Wright, and A St-Cyr. A guide to RBF-generated finite differences for nonlinear transport: Shallow water simulations on a sphere. *J. Comput. Phys.*, 231:4078–4095, 2012.

[12] D Stevens, H Power, Y Meng, C, D Howard, and K.A Cliffe. An alternative local collocation strategy for high-convergence meshless pde solutions, using radial basis functions. *J. Comput. Phy*, (submitted):–, 2012.

[13] X.Y. Cui, G.R. Liu, and G.Y. Li. A cell-based smoothed radial point interpolation method (cs-rpim) for static and free vibration of solids. *Engineering Analysis with Boundary Elements*, 34:144–157, 2010.

[14] A.T. Mahyari. *Computational Modelling of Fracture and Damage in Poroelastic Media.* PhD thesis, McGill Unniversity, Montreal, Quebec, Canada, 1997.

[15] L.M. Kachanov. Time of rupture process under creep conditions. *Izv. Akad. Nauk. SSR Otd. Teck*, 8:26–31, 1958.

[16] D Krajinovic and G.U. Fonseka. The continuous damage theory of brittle materials - part I: General theory. *ASME J. Appl. Mech.*, 48:809–815, 1981.

[17] J.C. Simo and J.W. Ju. Strain and stress based continuum damage models ii: Computational aspects. *International Journal of Solids and Structure*, 23:841–869, 1987.

[18] A.P.S Selvadurai and M.C. Au. Damage and visco-plasticity effects in the indentation of a polycrystalline solid. In *Proceedings of Plasticity 91: 3rd International Symposium on Plasticity and Its Current Applications, London*, 1991.

[19] H. Cheng and M.B. Dusseault. Deformation and diffusion behaviour in a solid experiencing damage: A continuous damage model and its numerical implementation. *International Journal of Rock Mechanics and Mining Sciences and Geomechanics Abstracts*, 30:1323–1331, 1993.

[20] J. Hu and A.P.S. Selvadurai. Influence of tertiary creep on the uplift behaviour of a pipe embedded in a frozen soil. In *Second International Conference on Advances in Underground Pipeline Engineering, Seattle*, 1995.

[21] N.G.W Cook. Failure of rock. *International Journal of Rock Mechanics and Mining Sciences and Geomechanics Abstracts*, 2:289–403, 1965.

[22] Z.T Bieniawski, H.G Denkhaus, and U.W Vogler. Failure of fractured rock. *International Journal of Rock Mechanics and Mining Sciences and Geomechanics Abstracts*, 6:323–346, 1967.

[23] M.D. Zoback and J.D. Byerlee. The effect of microcrack dilatancy on the permeability of westerly granite. *Journal of Geophysical Research*, 80:752–755, 1975.

[24] H.R. Samaha and K.C. Hover. Influence of microcracking on the mass transport properties of concrete. *ACI Materials Journal*, 89:416–424, 1992.

[25] L. Shiping, L. Yushou, L. Yi, W. Zhenye, and Z. Gang. Permeability-strain equations corresponding to the complete stress-strain path of yinzhuang sandstone. *International Journal of Rock Mechanics and Mining Sciences and Geomechanics Abstracts*, 31:383–391, 1994.

[26] S.Y. Wang, L. Sun, A.S.K. Au, T.H. Yang, and C.A. Tang. 2d numerical analysis of hydraulic fracturing in heterogeneous geo-materials. *Construction and Building Materials*, 23:2196–2206, 2009.

[27] M.A Biot. General theory of three dimensional consolidation. *Journal of Applied Physics*, 12:155–164, 1941.

[28] A Shirazi and A.P.S Selvadurai. Lateral loading of a rigid rock socket embedded in a damage-susceptible poroelastic solid. *International journal of geomechanics*, 5:276–285, 2005.

[29] Z. Wu. Hermite-Birkhoff interpolation of scattered data by radial basis functions. *Approximation Theory and its Applications*, 8:1–11, 1992.